American Mineralogist, Volume 84, pages 1915–1924, 1999

Silicate and oxide exsolution in pseudo-spinifex olivine from metaultramafic rocks of the Betic Ophiolitic Association: A TEM study

M.D. RUIZ CRUZ,[1,*] E. PUGA,[2] AND J.M. NIETO[3]

[1]Departamento de Química Inorgánica, Cristalografía y Mineralogía, Facultad de Ciencias, Universidad de Málaga, 29071 Málaga, Spain
[2]Instituto Andaluz de Ciencias de la Tierra (CSIC-UGRA), Facultad de Ciencias, Avenida Fuentenueva s/n, 18002 Granada, Spain
[3]Departamento de Geología, Facultad de Ciencias Experimentales, Universidad de Huelva, 21819 Palos de la Frontera, Huelva, Spain

ABSTRACT

Transmission electron microscopy (TEM) has been used to study submicroscopic particles in spinifex-like textured olivine from secondary harzburgites collected from the Cerro del Almirez locality in the Mulhacén Complex (Betic Cordillera, SE Spain). Three main types of submicroscopic oxides have been identified: (1) equidimensional Fe-rich spinel (magnetite), with average grain size in the order of 1–2 μm; (2) elongated Cr-bearing spinels (Fe-chromite to Cr-magnetite) with sizes ranging from 0.2 to 1 μm long and 0.01 to 0.1 μm thick; and (3) equidimensional Ti-rich particles from <0.01 to 0.1 μm and compositions ranging from ilmenite to Fe-Cr-Ti oxide. Chromite and ilmenite particles form parallel, chromite-rich and ilmenite-rich bands, extending along the **a**-axis of the host olivine. Both phases show a fixed orientation relationship with olivine, with the approximately hexagonal close-packed oxygen planes being parallel in both structures. These textural relationships indicate that both chromite and ilmenite were formed during a common exsolution process. Magnetite particles also are orientated preferentially relative to the olivine, but these particles are homogeneously distributed within the olivine, suggesting either a primary origin or an exsolution process that was not contemporaneous with formation of chromite and ilmenite.

Chromite particles commonly are accompanied by lamellae of talc and/or enstatite, both showing a consistent orientation relationship with olivine. Talc lamellae are twice as thick as the associated chromite crystals, whereas enstatite lamellae show a greater thickness and, moreover, form single enstatite particles, which consist of clino- and orthoenstatite intergrowths. Talc formation may be explained by exsolution, together with spinel, from olivine containing OH-groups, probably related to incomplete dehydration of serpentine during olivine formation. On the basis of these results and previously reported petrological data, we have concluded that exsolution of chromite-silicate and ilmenite occurred during the retrograde stage that followed the climax of the eo-Alpine metamorphic event.

INTRODUCTION

Different types of non-primary oxide inclusions, commonly associated with silicate phases, have been described in olivine and formed by different exsolution mechanisms (Goode 1974; Gooley et al. 1974; Kohlstedt and Vander Sande 1975; Putnis 1979; Moseley 1984; Otten 1985; Banfield et al. 1990). Several different types of oxide-silicate exsolutions may be distinguished on the basis of their size, concentration, and distribution within the host olivine, textural relationships between oxide and silicate, and composition of both oxide and silicate phases.

The best known oxide-silicate precipitates are the coarse (up to 5×100 μm) worm-like intergrowths (symplectites), which commonly show the association of spinel (mainly chromite or magnetite) with a Ca-rich (diopside or augite) or an Mg-rich (enstatite or hypersthene) pyroxene (Haggerty and Baker 1967; Gooley et al. 1974; Arai 1978; Putnis 1979; Moseley 1984). Submicroscopic spinel-pyroxene intergrowths with similar mineral associations have also been described (Otten 1985), where the spinel shows either dendritic or euhedral forms. In a few cases, the phase associated with the spinel is amorphous or crystalline silica (Kohlstedt and Vander Sande 1975; Banfield et al. 1990). The association spinel-fluid phase (CO_2) has also been reported (Green and Gueguen 1983).

Another set of papers describes Ti-, Cr-, and Fe-bearing particles where the associated silicate phase either is lacking or has not been observed (Ashworth 1979; Moseley 1981; Drury and Van Roermund 1988; Dobrzhinetskaya et al. 1996; Risold et al. 1997; Hacker et al. 1997; Ulmer and Trommsdorff 1997), although in some cases two different oxide phases, spinel and ilmenite, appear either as separate or as composite precipitates (Dobrzhinetskaya et al. 1996; Green et al. 1997).

The observed development of Cr-Fe oxides together with a silicate phase during the exsolution process agrees with the results of heating experiments of natural olivine of variable composition (Champness and Gay 1968; Champness 1970),

*E-mail: mdruiz@uma.es

indicating that breakdown of the olivine structure, at increasing temperature, produces two anhydrous silicate phases, silica and pyroxene, together with Fe-oxide.

The formation of hydrous silicates such as amphiboles or sheet silicates (mainly talc, chlorite, serpentine, and smectite), is clearly related to hydration reactions occurring either during retrograde metamorphism or during hydrothermal and low-temperature alteration. These types of processes have been investigated extensively by Baker and Haggerty (1967), Veblen et al. (1977), Veblen and Burnham (1978), Veblen and Buseck (1980), and Banfield et al. (1990).

The identification of a hydrous phase (talc) together with enstatite, associated with Cr-Fe-spinel in olivine from the Betic Ophiolitic Association (BOA) ultramafic rocks (Puga et al. 1998) is extremely interesting because of its mineralogical and petrological implications. In fact, processes that differ from the secondary hydration of pyriboles must be invoked in this case for talc formation from olivine. On the basis of petrological data, the establishment of both the physical conditions and time constraints on talc formation will allow a more accurate interpretation of the origin of the hydroxyl, as well as of the metamorphic conditions that affected the BOA ultramafic rocks.

GEOLOGICAL SETTING AND PETROLOGICAL DATA

The silicate and oxide particles occur in olivine from secondary harzburgites, which are part of the ultramafic sequence of the BOA in the Mulhacén Complex (Puga 1990; Puga et al. 1999). The samples come from the Cerro del Almirez, in Sierra Nevada (Fig. 1), which forms part of the Mulhacén Complex (Betic Cordillera, SE Spain). This Complex crops out as tectonic windows placed below the Alpujarride Complex and above the Veleta Complex (Fig. 1). This outcrop, about 3 km in length and several hundred meters thick, consists of antigorite serpentinites containing numerous dikes from 0.1 to 1 m wide, and boudins of partly eclogitized rodingite.

The secondary harzburgites originally were the most abundant lithotype in this ultramafic ophiolitic sequence. The harzburgites are metamorphic rocks derived from spinel lherzolites, through the following sequence of petrogenetic processes, which have been documented in Puga et al. (1999).

(1) An oceanic serpentinization stage of the lherzolites, giving rise to their local transformation into aggregates of chlorine-bearing serpentine and chlorite and oxide minerals. These aggregates enclose relics of mantle-derived olivine, whose representative composition is reported in Table 1. This initial

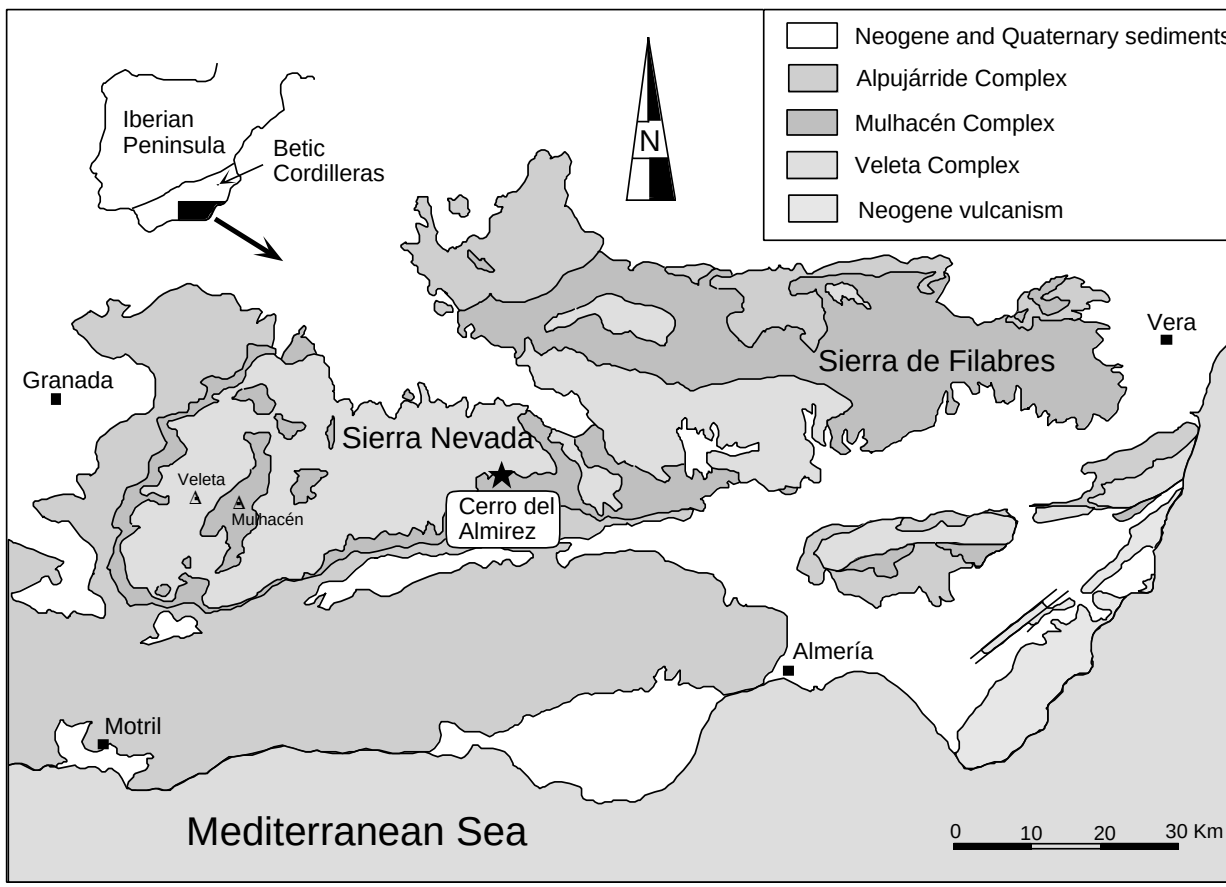

FIGURE 1. Geological sketch map of the central-eastern sector of the Betic Cordillera, showing some of its constituent metamorphic complexes that formed during the Alpine Orogeny. Star represents the location of the meta-ophiolitic ultramafic-rodingite association of the Cerro del Almirez outcrop. Limits between complexes according to geological maps 1:50.000 from MAGNA series and Diaz de Federico's unpublished data.

TABLE 1. Representative microprobe analyses of the mineral phases shown in Figure 2

		Spinifex-like olivine					
	Mantle-derived olivine relic	Intermediate dark -brown zone	Light-brown core	Colorless rim	Opx	Chl	Mag
SiO_2	41.30	40.77	40.85	40.64	58.43	33.81	0.01
TiO_2	0.01	0.03	0.11	—	0.02	0.03	0.44
Al_2O_3	0.01	0.01	—	—	0.06	14.30	0.28
Cr_2O_3	—	0.26	0.01	—	0.02	1.44	9.78
FeO	9.30	8.68	9.06	9.24	6.28	3.22	80.81
MnO	0.21	0.11	0.11	0.11	0.17	—	0.17
NiO	0.28	0.42	0.48	0.37	0.10	0.30	0.56
MgO	49.40	49.88	49.73	49.69	35.50	33.94	1.71
CaO	0.01	—	—	—	0.05	—	—
Na2O	0.05	—	0.01	—	0.02	0.03	0.02
K2O	0.02	0.02	0.02	—	0.01	0.03	—
F	—	0.06	0.15	—	0.04	0.37	0.20
Cl	0.01	—	0.01	—	—	0.04	0.01
Total	100.59	100.23	100.54	100.05	100.68	87.50	93.99
			Formula proportions of cations*				
Si	1.00	1.00	1.00	0.99	2.00	6.39	—
^{IV}Al	—	—	—	—	—	1.61	—
^{VI}Al	—	—	—	—	—	1.57	0.10
Ti	—	—	—	—	—	—	0.10
Cr	—	0.01	—	—	—	0.21	2.34
Fe^{3+}	—	—	—	0.01	0.01	—	13.55
Fe^{2+}	0.19	0.17	0.18	0.18	0.17	0.51	6.93
Mn	—	—	—	—	—	—	0.04
Ni	0.01	0.01	0.01	0.01	0.00	0.05	0.14
Mg	1.79	1.81	1.81	1.81	1.81	9.56	0.77
Ca	—	—	—	—	—	—	—
Na	—	—	—	—	—	0.01	0.01
K	—	—	—	—	—	0.01	—

* Based on 4 oxygen atoms for olivine, 6 oxygen atoms for orthopyroxene, 28 oxygen atoms for chlorite, and 32 oxygen atoms for magnetite.

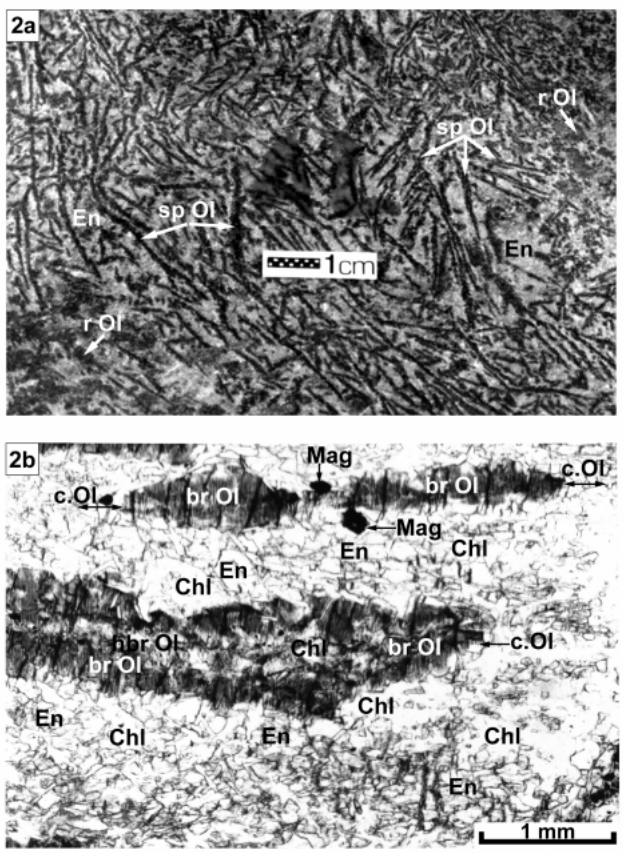

serpentinization process was contemporaneous with (and complementary to) alteration that partly transformed the dolerite dikes that crosscut the ultramafic rocks into rodingites.

(2) A high-pressure metamorphism of the partly serpentinized lherzolites under eclogite facies conditions, during an eo-Alpine subduction process, which also affected the plutonic, volcanic, and sedimentary sequences of the BOA. In this eo-Alpine metamorphic event, the previously formed phyllosilicates were replaced by a brown olivine, with spinifex-like texture (Fig. 2a), containing rare inclusions of (K,Na)Cl. This brown olivine occurs in a paragenesis with enstatite and minor Cr-chlorite and Cr-magnetite, forming the secondary harzburgite. The chemical compositions of the main minerals in this rock type are reported in Table 1. The spinifex-like textured olivine commonly shows an irregular light brown core, surrounded by a thicker dark-brown zone, and a discon-

FIGURE 2. (**a**) Macroscopic aspect of a secondary harzburgite with spinifex-like textured olivine crystals (sp Ol), dark in the photo, surrounded by a matrix of needle-like enstatite aggregates (En). Some rounded relics of mantle-derived olivine (r Ol) are preserved in this ultramafic rock and locally appear overgrown by the more abundant spinifex-like olivine crystals. (**b**) Brown olivine crystals with spinifex-like texture surrounded by an enstatite (En) and chlorite (Chl) matrix, which contains some microscopic magnetite grains (Mag). Olivine crystals in this plane-polarized light photograph are elongated parallel to b-axis and show a thin, light-brown core (l br Ol) and a discontinuous, colorless rim (c. Ol).

tinuous colorless rim (Fig. 2b). In the brown zones of the olivine (Table 1), $TiO_2 + Cr_2O_3$ may reach 0.5 wt% and, exceptionally, up to 1 wt% (Puga et al. 1999). In contrast, in the colorless rims, concentrations of Cr_2O_3 and TiO_2 are below detection limits for microprobe analysis (Table 1), which are 0.032 wt% for Cr and 0.0082 wt% for Ti.

(3) After a decompressional stage, which resulted in the partial exhumation and retrogression of the eclogitized ophiolites, a meso-Alpine metamorphic event affected these lithotypes and transformed them under *P-T* conditions corresponding to the albite-epidote amphibolite facies. During this metamorphic event, the residual meta-lherzolites were serpentinized, in a continental environment, while in the locally formed harzburgites, the spinifex olivine was probably overgrown by the colorless rim (Fig. 2b), and slightly replaced by chlorite and serpentine, whereas the enstatite was partly pseudomorphed by talc.

EXPERIMENTAL METHODS

From the optical study, a set of olivine grains, showing different orientations, were selected for the TEM study. Selected areas included variously colored olivine zones. Samples were prepared from thin sections in which washers were attached to the selected areas and later separated from the glass backing. These areas were ion-milled, carbon-coated, and examined in a 200-kV Philips CM-20 scanning-transmission electron microscope (STEM) fitted with an EDAX ultrathin window, solid-state Si(Li) detector for energy-dispersive X-ray analysis. Quantitative X-ray microanalysis was carried out using the thin-film approximation of Cliff and Lorimer (1975). Standards were natural albite for Na, natural muscovite and biotite for K, natural albite, spessartite and muscovite for Al, natural olivine and biotite for Mg and Fe, natural spessartite for Mn, and natural titanite for Ca and Ti. Interpolation between Mn and Ti values were used for the Cr correction factor.

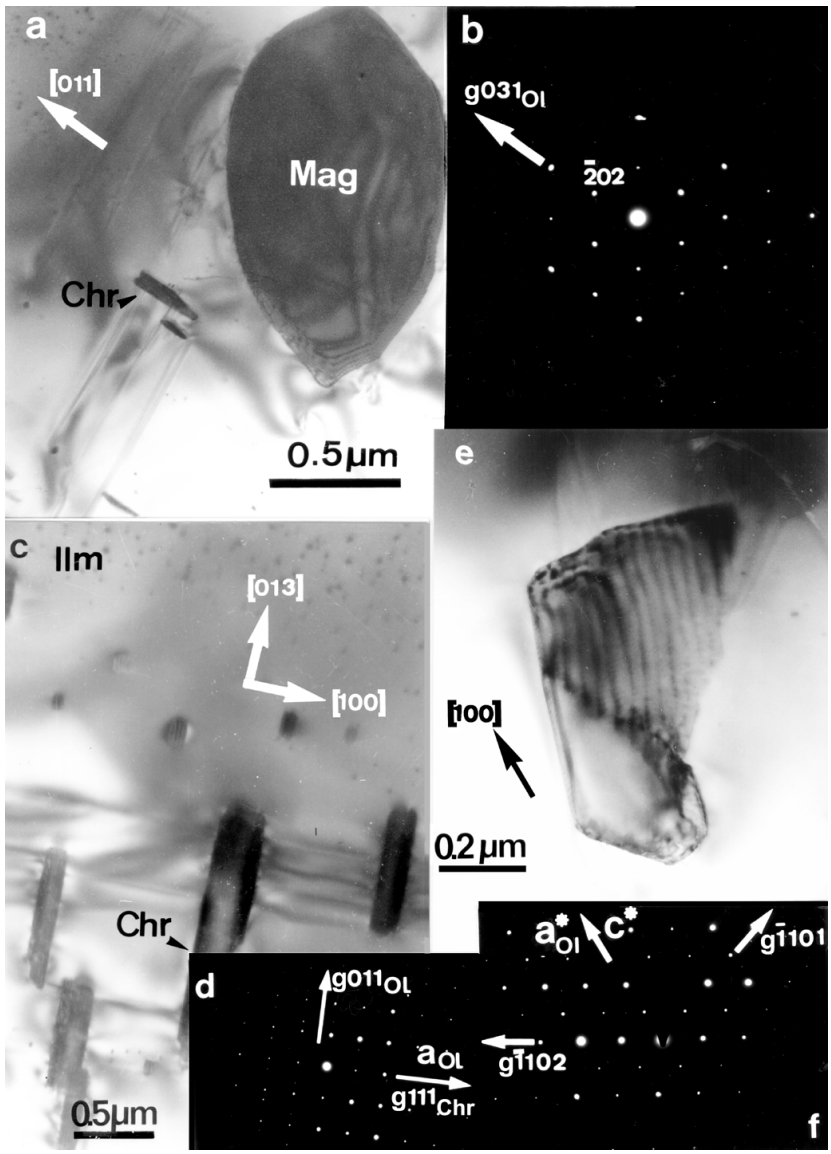

FIGURE 3. TEM images of the main types of submicroscopic oxide particles in the brown area of the spinifex-like textured olivine. (**a**) Electron micrograph showing the relative sizes of the magnetite (Mag), chromite (Chr), and ilmenite particles, the latter being abundant in the upper left corner. (**b**) SAED pattern of the magnetite [1$\bar{1}$1] zone axis. (**c**) Parallel bands of ilmenite (Ilm) and orientated chromite (Chr) particles. (**d**) The SAED pattern of the [0$\bar{1}$1] zone axis of olivine shows faint spots of chromite, which reveal the orientation relationships between the phases. (**e**) Electron micrograph showing one of the largest ilmenite particles that displays moiré fringes. (**f**) SAED pattern, of the [$\bar{1}\bar{1}$20] zone axis of ilmenite, showing the orientation relationships between host olivine and ilmenite. In **a** and **c**, planar defects parallel to the [100] direction of the olivine connect chromite particles.

TEM RESULTS

At the scale of TEM observation, the brown areas of the spinifex-like textured olivine shows oxide-mineral particles with a range of sizes (Puga et al. 1998): (1) equidimensional magnetite grains, with average grain size of ~1–2 μm; (2) subhedral, elongated spinel crystals, with sizes ranging from ~0.2 to 1 μm long and 0.01–0.1 μm thick, and compositions ranging from Fe-chromite to Cr-magnetite; and (3) small (<0.01–0.1 μm), equidimensional and commonly rounded grains with compositions ranging from ilmenite to Fe-Cr-Ti-oxide (Fig. 3). In this work we use the name "chromite" for the complete range of Cr-bearing spinels, whereas the name "ilmenite" includes Fe-Ti particles that might also contain Cr.

Low-magnification observations reveal that both chromite and ilmenite particles form parallel chromite-rich and ilmenite-rich bands a few micrometers in thickness, which extend along the **a**-direction of the host olivine (Fig. 3c). Planar defects, parallel to the [100] direction of olivine locally connect the chromite particles (Figs. 3a and 3c). In contrast, magnetite particles appear to be distributed homogeneously within the olivine grains. Chromite particles occur systematically forming parallel intergrowths with silicate phases, whereas this type of parallel intergrowth has not been observed for either magnetite or Ti-rich oxides.

Magnetite particles

The AEM data from the large equidimensional particles, such as those shown in Figures 3a and 4a, systematically contain large amounts of Fe and subordinate Cr, Mn, Ti, Ni, and V (Table 2). Most of the SAED patterns can be indexed as magnetite. Figure 3b shows the following orientation of magnetite with respect to the olivine: $(100)_{Ol}$ // $[111]_{Mag}$; $(010)_{Ol}$ // $[\bar{2}11]_{Mag}$; and $(001)_{Ol}$ // $[0\bar{1}1]_{Mag}$. These orientation relationships are the same as those reported previously for magnetite formed from olivine (e.g., Champness 1970). In some cases, diffraction patterns and high-resolution images of these crystals show a spacing of 14.3 Å (= $3d_{111}$ of magnetite), although the orientation with respect to the host olivine is maintained (Fig. 4b). These images could be interpreted as a moiré effect, although the presence of spots with a regular 14.3 Å spacing in the SAED patterns rather suggests the presence of a magnetite superstructure, which may be related either to cation (Fe and Cr) ordering in particles containing Cr, or to vacancy ordering, perhaps related to later oxidation of magnetite as in the maghemite structure

Chromite-silicate particles

The chromite-silicate lamellae are parallel to {111} of chromite, the interface with the olivine matrix being parallel to (100) of olivine. Chromite crystals display the same orientation relative to the host olivine as magnetite particles and appear frequently to consist of two or more twinned lamellae (Fig. 5). A superstructure with a spacing of 14.3 Å, similar to that in magnetite particles, is commonly observed on the outer parts of the chromite crystals.

The chromite particles show a wide compositional range (Table 2), with Fe^{3+} contents ranging from 0.36 atoms per formula unit (apfu) (ferroan chromite) to 1.56 apfu (chromian magnetite). Most of the analyses appear to be "contaminated"

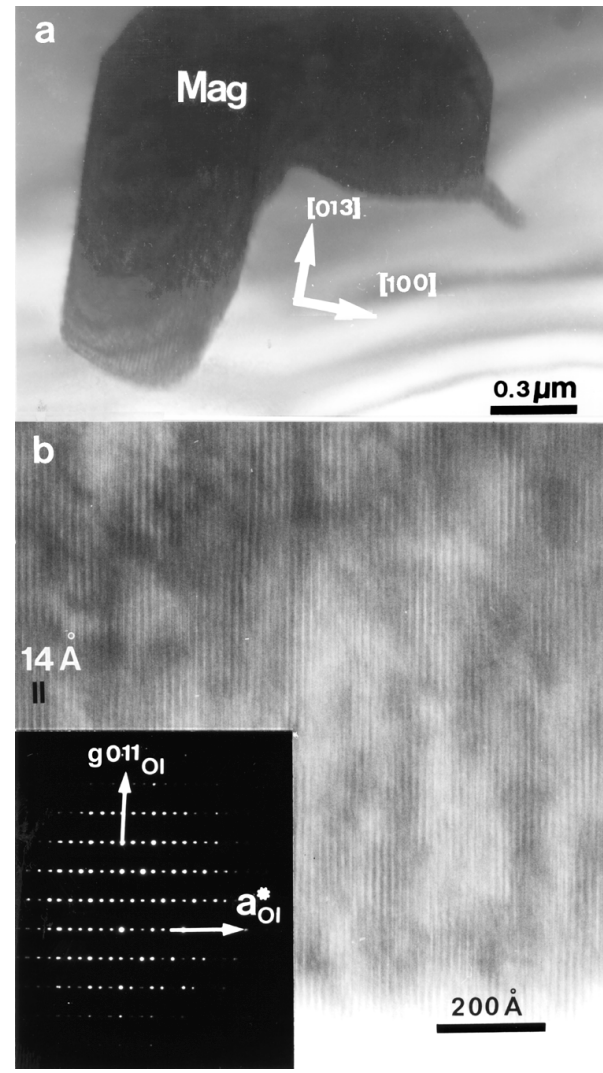

FIGURE 4. (**a**) Image of a large magnetite particle. (**b**) The high-resolution image shows fringes with spacing = 14.3 Å. The SAED pattern (inset) of the [011] zone axis of the olivine, also shows the 14.3 Å spacing (= $3d_{(111)}$ of magnetite).

by the enclosing olivine, and the formulae have been recalculated by removing Si together with Mg and Fe in the proportions indicated by the olivine analyses.

There are two main types of silicate phases in many cases associated with chromite: one shows light contrast resulting from rapid beam damage (Fig. 6a), whereas the other maintains contrast similar that of host olivine (Fig. 6b). The second type of silicate is also observed as isolated particles, without parallel oxide crystals.

Because of the small sizes of the particles, analyses of the silicate phases in many cases appear to be contaminated by adjacent chromite or olivine, and their identification is very difficult on the basis of the AEM data alone. An estimate of the degree of olivine contamination may be obtained from the (Si+Al)/(Fe+Mg) ratio, which ranges from 0.44 to 0.48 in the

TABLE 2. AEM data for oxide particles (in cation%)

	Magnetite		Chromite								Ilmenite		
	Fig. 3	Fig. 4	Fig. 3			Fig. 5	Fig. 6a		Fig. 6b	n.s.	Fig. 3c	Fig.3e	n.s.
Si	–	–	2.12	9.12	8.79	3.05	16.54	11.30	13.18	21.11	12.64	1.70	–
Al	–	0.57	1.03	0.80	–	0.96	–	1.46	–	–	–	–	–
Fe	92.89	78.73	56.19	47.97	32.78	44.09	33.49	33.89	31.08	33.22	31.40	38.83	35.04
Mg	–	1.05	5.50	19.55	18.68	7.16	16.73	26.20	26.76	40.72	29.79	11.00	10.40
Mn	2.02	0.04	–	–	–	–	–	–	–	–	–	0.60	0.65
Ti	–	0.77	0.80	1.20	0.61	1.20	–	0.93	0.57	–	23.53	47.87	53.91
Cr	3.98	18.40	34.36	21.36	39.14	43.54	33.24	26.22	28.41	5.02	2.64	–	–
Ni	1.11	0.44	–	–	–	–	–	–	–	–	–	–	–
Formula proportions of cations*													
Al^{3+}	–	0.07	0.03	0.03	–	0.03	†	0.07	–	–	–	–	–
Cr^{3+}	0.12	0.55	1.10	0.91	1.61	1.43	†	1.24	1.41	0.44	0.09	–	–
Ti^{4+}	–	0.02	0.03	0.05	0.03	0.04	†	0.04	0.03	–	0.77	1.01	1.08
Fe^{3+}	1.85	1.35	0.83	1.01	0.36	0.49	†	0.64	0.55	1.56	–	–	–
Fe^{2+}	0.94	1.01	0.94	0.94	0.94	0.97	†	0.88	0.88	1.00	0.95	0.82	0.70
Mg^{2+}	–	0.03	0.05	0.06	0.06	0.04	†	0.13	0.06	–	0.19	0.16	0.21
Mn^{2+}	0.06	–	–	–	–	–	†	–	–	–	–	0.01	0.01
Ni^{2+}	0.03	0.02	–	–	–	–	†	–	–	–	–	–	–
O	4	4	4	4	4	4	†	4	4	4	3	3	3

Notes: Structural formulae have been recalculated by removing Si, Fe, and Mg, in a ratio similar to that determined in the host olivine. n.s.: analyses from particles not shown in the figures.
* Based on three oxygen atoms for ilminite, and four oxygen atoms for magnetite and chromite.
† Analysis contaminated with both olivine and talc.

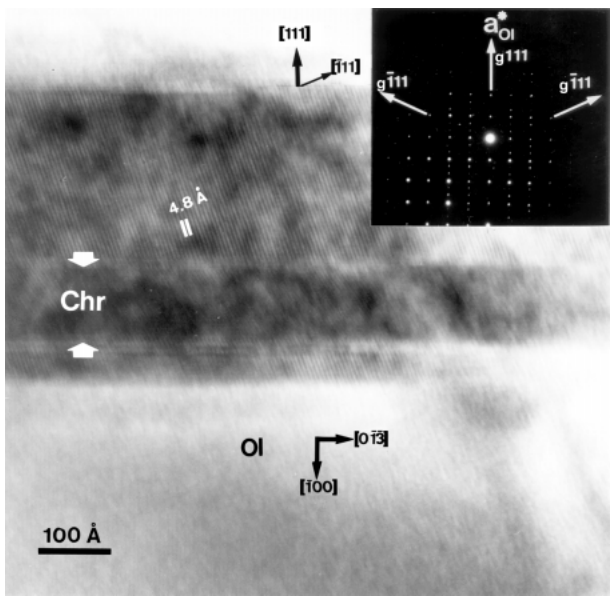

FIGURE 5. High-resolution image of a chromite particle (Chr), elongated along the [013] direction of olivine (Ol). The darker lamella (between the white arrows) is a twin. The topotactic relations between chromite and olivine are revealed by the SAED pattern (inset), of the [0$\bar{1}$1] zone axes of olivine and chromite.

analyzed olivine (Table 3). Nevertheless, information provided by the complex SAED patterns and the high-resolution images has permitted the identification of two types of Mg-rich silicate, talc and enstatite, which correspond respectively to the beam-sensitive and beam-stable particles. Both minerals generally coexist within the chromite-rich bands, although it is not unusual to observe areas in which either talc or, less commonly, enstatite predominates.

Chromite-talc particles. Chromite-talc particles appear as parallel intergrowths, the talc lamellae showing a thickness approximately double that of the associated chromite lamellae (Fig. 6a). High-magnification electron micrographs of these crystals permit only occasional imaging of the 9.3 Å fringes of talc, because of the rapid rate with which it suffers electron beam damage (Veblen and Buseck 1980). Figure 6a also shows the orientation relationships among chromite, talc, and host olivine. The SAED pattern shows the [0$\bar{1}$1] zone axis of olivine and the [$\bar{3}$10] zone axis of talc, and reveals the following orientation relationships between both phases: $(100)_{Ol}$ // $(001)_{Tlc}$; and $[011]_{Ol}$ // $[310]_{Tlc}$. This pattern also reveals the lack of exact coincidence between the (13*l*) and (*hkk*) rows of the two phases.

AEM data from talc lamellae are reported in Table 3, together with those of the host olivine. Contamination with either chromite or olivine is revealed, respectively, by the Cr content and the Si/(Fe+Mg) ratio. Structural formulae have been calculated only when this ratio is close to the ideal value for talc (>1.33).

Enstatite and chromite-enstatite particles. Enstatite particles either are associated with chromite crystals (Fig. 6b) or occur as single lamellae (Figs. 6b and 7), the latter generally showing a greater thickness. As a consequence the observed enstatite/chromite ratio is notably higher than the talc/chromite one. The chromite-enstatite intergrowths are, in some cases, parallel to the shortest dimension of these crystals and are similar to those formed by talc and chromite (Fig. 6b). However, very elongated enstatite lamellae, growing along the longest direction of the particles, are also observed.

High-resolution images of enstatite commonly show areas with 9 Å fringes and areas with 18 Å fringes (Fig. 7). These spacings correspond, to the **a**-dimensions of clinoenstatite and orthoenstatite, respectively. Similar **b**-axis images were described by Iijima and Buseck (1976) and interpreted as intergrowths of orthoenstatite (OREN) and clinoenstatite (CLEN). Topotactic relations between the two polymorphs and

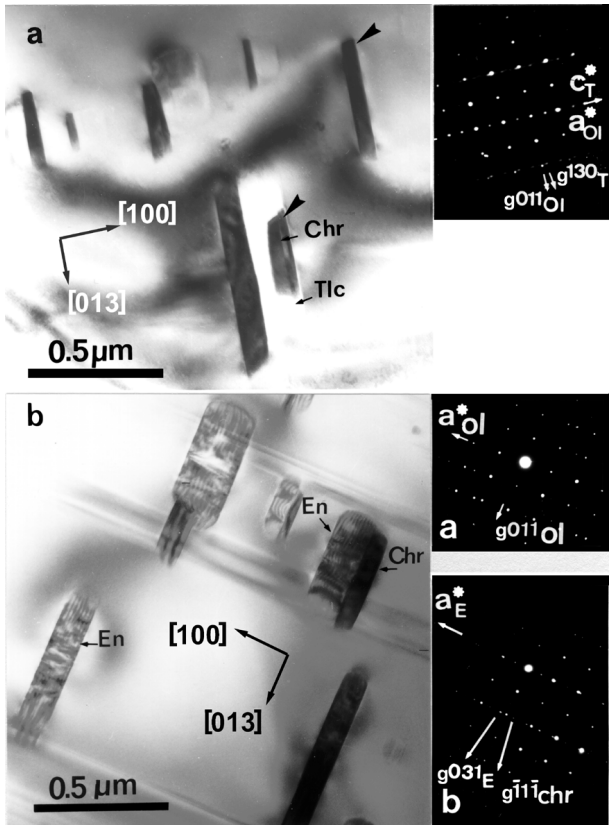

FIGURE 6. TEM images of chromite-silicate intergrowths. (**a**) Chromite (Chr)-talc (Tlc) particles. The SAED pattern (inset) of the [0$\bar{1}$1] zone axis of olivine and [$\bar{3}$10] zone axis of talc reveals the 9.3 Å basal spacing of talc, and the different spacing of the 13*l** rows of talc and the *hkk** rows of olivine. (**b**) Chromite (Chr)-enstatite (En) and enstatite particles. SAED a shows the [0$\bar{1}$1] zone axis of olivine and SAED b, down the [0$\bar{1}$3] zone axis of the pyroxene, shows the 9 Å spacing of clinoenstatite (corresponding to the (100) reflections). The *h*31* rows of clinoestatite coincide with the *hkk** rows of olivine. (In the SAED patterns, T = Talc, and E = Enstatite).

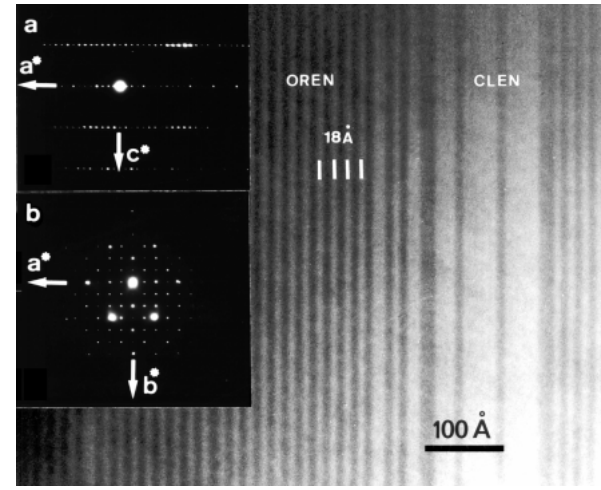

FIGURE 7. High-resolution image of an enstatite particle with dominant 18 Å fringes (OREN), and rarer lamellae showing 9 Å fringes (CLEN). The SAED patterns show (**a**) the [010] and (**b**) the [001] zone axes of orthoenstatite, the former corresponding with the image.

the host olivine, illustrated by the SAED patterns (Figs. 6b and 7) are: $(100)_{Ol}$ // $(\bar{1}00)_{OREN}$ // $(100)_{CLEN}$; $[011]_{Ol}$ // $(010)_{OREN}$ // $(010)_{CLEN}$; and $[0\bar{1}3]_{Ol}$ // $(001)_{OREN}$ // $(001)_{CLEN}$. The elongation of the enstatite lamellae coincides with the direction of the silicate chains, the **c**-direction in the pyroxene structure.

AEM data from enstatite lamellae (Table 3) indicate Si/(Fe+Mg) ratios <1, which can be explained either by olivine contamination, mainly in the case of thin lamellae, or by replacement of Si by Fe^{3+}, in the tetrahedral positions. This is probably the case of the large lamella shown in Figure 7, where contamination with host olivine is unlikely.

Textural relations among chromite, talc, and enstatite. Figure 6 shows two examples of chromite-rich bands, where the associated silicate is, respectively, talc and enstatite. Nevertheless, it is common to observe chromite bands showing parallel intergrowths of chromite with both talc and enstatite. The SAED patterns obtained in these areas (not shown) reveal the coincidence of the [001] zone axis of enstatite and the [100] zone axis of talc. These images show that enstatite and talc lamellae grow preferentially on opposite sides of the chromite crystals or, alternatively, the two phases are separated by host olivine.

Ilmenite particles

The most characteristic features of the ilmenite particles are their small size, generally <0.03 µm, and the presence of moiré fringes (Figs. 3a, 3c, and 3e). The orientation relationships between ilmenite and olivine (Fig. 3f) are: $(100)_{Ol}$ // $(0001)_{Ilm}$; $(010)_{Ol}$ // $[01\bar{1}0]_{Ilm}$; and $(001)_{Ol}$ // $[\bar{1}230]_{Ilm}$. Analyses of ilmentite typically contain a substantial contribution from the olivine host (Table 2); the probable composition of the ilmenite precipitates was calculated, as for chromite particles, by removing Si from the analyses, along with Mg and Fe in the proportions in which they are present relative to Si in olivine. The derived formulae show (Fe+Mg)/Σcations ratios ranging from 0.46 to 0.57. Nevertheless, some of the derived formulae do not correspond to ilmenite, but to an undetermined Fe-Cr-Ti oxide.

DISCUSSION

Origin of oxide particles

Three main types of submicroscopic oxide particles have been identified in olivine from the BOA ultramafic rocks: magnetite, chromite, and ilmenite. Magnetite particles occur in both the light-brown core and the darker brown area of the olivine, and they are not accompanied by a silicate phase; both facts suggest that the magnetite either has a primary origin or formed by an exsolution process that was not contemporaneous with the formation of ilmenite and chromite. Silicate phases have not been identified with ilmenite particles, due either to their small size or the fact that they are absent. Nevertheless, spatial relations between chromite-rich and ilmenite-rich bands suggest that the two types of oxide-mineral associations were formed during a common exsolution process.

TABLE 3. AEM data for olivine and other silicate particles (in cation%)

	Olivine				Talc				Enstatite				
	Fig. 3	Fig. 6a	Fig. 6b	n.s.	Fig. 6a		n.s.		Fig. 6b	Fig. 7	n.s.	n.s.	
Si	31.33	30.68	31.96	32.20	58.94	48.68	58.95	49.96	41.97	47.00	34.59	40.63	37.00
Al	–	–	–	–	–	–	0.46	–	–	–	–	–	–
Fe	6.47	6.16	6.26	6.36	6.80	7.53	3.88	3.77	5.94	4.89	6.05	5.12	6.17
Mg	62.20	63.16	61.78	61.44	34.26	42.68	36.71	46.27	52.09	48.11	59.36	54.25	56.83
Cr	–	–	–	–	–	1.11	–	–	–	–	–	–	–
(Si+Al)/(Fe+Mg)	0.46	0.44	0.47	0.48	1.43	0.95	1.43	1.02	0.72	0.89	0.53	0.68	0.59
					Formula proportions of cations*								
^{IV}Si	0.95	0.93	0.96	0.97	4.07		4.06			0.95			
^{VI}Fe	0.20	0.20	0.19	0.19	0.48		0.27			0.10			
^{VI}Mg	1.89	1.93	1.85	1.85	2.37		2.58			0.97			

Notes: Structural formulae of talc and enstatite have been calculated only for uncontaminated analyses. n.s.: analyses from particles not shown in the figures.
* Based on 4 oxygen atoms for olivine, 11 oxygen atoms for talc, and 3 oxygen atoms for enstatite.

Two main processes have been invoked to explain oxide-mineral exsolution in olivine: (1) Fe oxidation, in a wide temperature interval, which mainly would lead to exsolution of Fe^{3+}-bearing oxides (hematite or magnetite) (Goode 1974; Kohlstedt and Vander Sande 1975; Putnis 1979; Banfield et al. 1990). (2) Direct exsolution of high-charge cations (Ti^{4+}, Cr^{3+}, Fe^{3+}) as temperature and pressure decrease (Moseley 1981, 1984; Dobrzhinetskaya et al. 1996; Ulmer and Trommsdorff 1997), which would form Ti^{4+}-, Cr^{3+}-, or Fe^{3+}-bearing oxide minerals. Although the two processes are clearly different, they yield identical orientation relationships. Moreover, both processes may occur simultaneously, as in some examples of magnetite-diopside exsolution, where Ca liberation was probably accompanied by Fe oxidation (Otten 1985).

In the BOA spinifex-like textured olivine (Fig. 2b), the external chromite-free zone has been interpreted on the basis of the chemical data (low Ti and Cr contents in microprobe analyses) as an overgrowth that originated during a metamorphic stage after the exsolution process. On the other hand, the low Cr and high Ti contents of the internal zone can be explained by local variations in both Cr and Ti availability during the growth of some crystals (Puga et al. 1999). The local lack of the external particle-free rim indicates that chromite precipitates were abundant near the edges of the olivine prior to the rim development. This suggests that oxide exsolution was influenced by an oxidation process. Nevertheless, AEM data show that the Fe content in olivine is similar in both precipitate-rich and precipitate-poor areas, indicating that oxidation, if it took place, had not progressed far.

On the other hand, microprobe data (Puga et al. in preparation) suggest that the particle concentration controls the Cr content (Table 1), whereas AEM data of olivine from particle-rich areas (Table 3) shows that olivine does not now contain measurable Cr. This indicates that Cr was completely exsolved from the olivine structure. Moreover, the lack of pure magnetite in this type of exsolution also suggests that Cr liberation may have been the main factor controlling the exsolution process.

Interpretation of genetic conditions of silicate phases

Precipitates of exsolved chromite are systematically accompanied by precipitates of talc and/or enstatite. Talc has been reported frequently as an alteration product of enstatite and anthophyllite (Veblen and Buseck 1980, 1981) whereas the association talc-enstatite also has been interpreted as a retrograde metamorphic product of anthophyllite (Evans 1977; O'Hanley 1996). Nevertheless, in BOA olivine two observations indicate that precipitation of these phases was not preceded by anthophyllite. First, anthophyllite has not been identified in any of the numerous silicate particles analyzed. Second, talc and enstatite commonly develop in separated microdomains, and when they coexist have never been observed in contact. This suggests that both phases precipitated directly and independently, probably above the stability field of anthophyllite, as shown graphically in Figure 8. This figure represents a *P-T* grid of phase relations for the silicate phases relevant to this work, in the model system SiO_2-MgO-H_2O. The *P-T* grid was calculated assuming water and mineral activities equal to 1 and therefore should be taken to represent only the topology of the phase relations.

CLEN-OREN intergrowths, frequent in pyroxene exsolution lamellae (Buseck et al. 1980) may form during crystal growth as well as by transformation of protoenstatite (PEN) at decreasing temperature, or by polymorphic transformation OREN → CLEN (Buseck and Iijima 1975). The application of the criteria proposed by Buseck and Iijima (1975) suggests that clinoenstatite formed by transformation from orthoenstatite, at moderate to low temperature. The physical conditions of this transformation are shown in Figure 8.

Talc commonly forms from pyriboles (Veblen and Buseck 1980, 1981) during hydration reactions. Nevertheless, in our case, possible H_2O input from phases adjacent to olivine, occurring during exsolution, did not affect the innermost parts of the olivine grains, as indicated by the observation that enstatite precipitates do not show any sign of transformation to talc; indeed, talc particles occur only in association with chromite. Therefore, we suggest two possible mechanisms for talc formation: (1) hydration reactions restricted to certain microdomains within the olivine grains and (2) direct exsolution of talc from olivine that contained OH-groups.

The first mechanism is suggested by the presence of locally abundant saline inclusions (NaCl and KCl) in olivine, which have been interpreted as the result of interaction of marine fluids with the ultramafic lithotypes during the oceanic serpentinization stage (Puga et al. 1999). This mechanism would require the solid in-

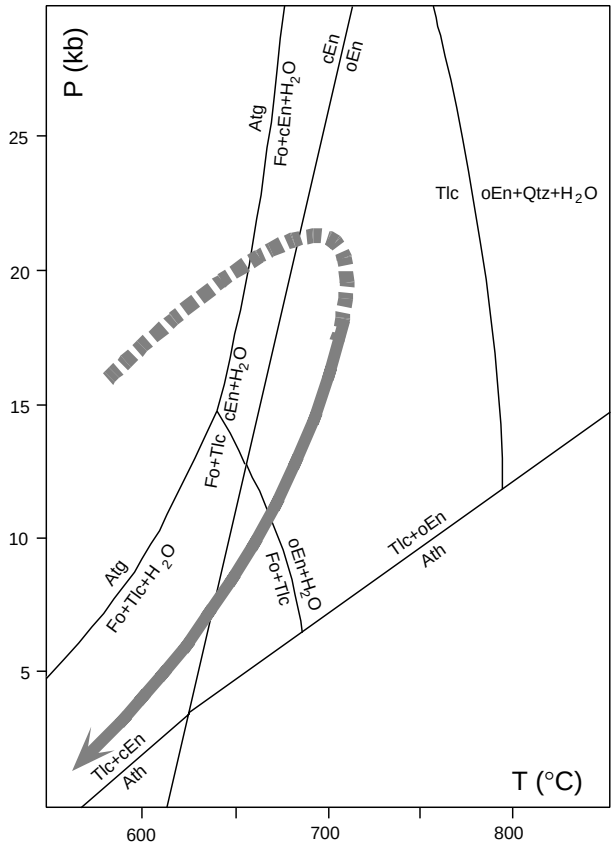

FIGURE 8. *P-T* diagram of selected silicate phases for the system SiO_2-MgO-H_2O calculated from the thermodynamic data of Berman (1988) using the computer program TWEEQU (Berman 1991). The arrow shows a possible *P-T* path defined by the observed mineral associations.

clusions to contain an aqueous phase that was subsequently liberated. Nevertheless, the associated alkali-rich phases that would result from this process have not been identified, suggesting that the saline fluids were probably lost before the trapping of the salts by the host olivine.

The second hypothesis implies that the olivine structure contained some OH-groups replacing oxygen. The presence of structural water in the form of OH-groups in olivine has been pointed out by several authors (e.g., Deer et al. 1962; Martin and Donnay 1972; Wilkins and Sabine 1973; Beran and Putnis 1983; Kitamura et al. 1987; Miller et al. 1987). In the BOA ultramafic rocks, the presence of water may be related to incomplete dehydration of serpentine during the formation of olivine by the antigorite breakdown reaction Ant = Fo + En + H_2O, which took place at >20 Kb and ~700 °C, corresponding to the eo-Alpine climax conditions (Puga et al. 1999). Exsolution of Ti, Cr, and Fe^{3+} must have occurred during cooling and decompression. Consequently, liberation of both high-charge cations and OH from the olivine structure is assumed to have occurred during the eo-Alpine retrograde metamorphic process (Fig. 8).

Most reactions proposed for the formation of spinel assume that trivalent cations occupy octahedral positions and may be written using the hypothetical component $R^{3+}_{4/3}SiO_4$ (Arai 1978). The reaction between this component and the fayalite component produces spinel + silica (reaction 1), whereas the contemporary reaction of silica with olivine would form pyroxene (Moseley 1984), according to reaction 2:

$$3R^{3+}_{4/3}SiO_4 + Fe^{2+}_2SiO_4 \rightarrow 2R^{3+}_2Fe^{2+}O_4 + 4SiO_2 \quad (1)$$

$$4SiO_2 + 4X_2SiO_4 \rightarrow 4X_2Si_2O_6 \quad (2)$$

where R^{3+} corresponds to $Cr^{3+}$and Fe^{3+}, and X stands for Mg and Fe^{2+}.

Assuming that reaction 1 is similar in both talc and enstatite formation, the following reaction 3 may be written for talc formation from silica and OH-olivine:

$$5SiO_2 + 3X_2SiO_{10/3}(OH)_{4/3} \rightarrow 2X_3Si_4O_{10}(OH)_2 \quad (3)$$

The spinel/silicate ratio obtained from reactions 1 and 2 is slightly lower than from reactions 1 and 3, and a notably lower amount of olivine is involved in the latter. In other words, reaction 3 would form fewer (or smaller) lamellae than reaction 2 or, alternatively, reaction 2 would form single pyroxene lamella in addition to those associated with chromite crystals. From the observed images, the textural relationships among chromite, talc, and enstatite indicate a cooperative nucleation and growth mechanism for the three phases, their respective formation probably being dependent on the availability of OH.

As pointed out above, silicate phases have not been observed in direct association with ilmenite precipitates. Analogous situations, observed in spinel exsolutions in olivine and garnet, seem to imply that cations such as Fe^{3+} or Cr^{3+} can substitute for Si in the tetrahedral sites (Ashworth 1979; Brearley and Champness 1986). Similarly, the lack of a silicate phase as a reaction product of exsolved ilmenite may be explained if Ti occupies the tetrahedral positions in the olivine structure (Moseley 1981). In this case, liberation in similar proportions of Ti and Fe would require the development of a second oxide phase. However, the necessity for the second phase may be alleviated, through several mechanisms (Moseley 1981). These include the exsolution of non-stoichiometric ilmenite ($Fe_{1+x}Ti_{1-x}O_3$), which implies the presence of some Fe^{3+} in the olivine, and the simultaneous formation of ilmenite and chromite/magnetite precipitates. Nevertheless, the lack of an associated oxide may be explained by the following mechanism: the parallel exsolution, in a limited extent, of both Ti and Fe, respectively from the tetrahedral and the octahedral positions, would produce olivine with a deficit of Si and a parallel excess of (Fe+Mg), according to the following reaction:

$$X_2(Si_{1-x}Ti_x)O_4 \rightarrow Ti_xO_{3x}Fe_x + X_{2-x}Si_{1-x}O_{4-3x} \quad (4)$$

If the x values are on the order of 0.05, the resultant olivine composition is similar to that determined from the AEM data in Table 3, which requires that some Fe be trivalent in the tetrahedral positions.

ACKNOWLEDGMENTS

The authors are very grateful to A. Brearley (University of New Mexico), P. Champness (University of Manchester), B. Evans (University of Washington), F. Nieto (University of Granada), A. Putnis (University of Münster), and D.R. Veblen (Johns Hopkins University) whose corrections and suggestions have

notably improved the manuscript. The authors are also grateful to M.A. Abad for help in obtaining the TEM/AEM data, and to A. Diaz Puga and A. Molina for the performance of the photos. Financial support from Spanish Project PB 95-0220 and from the Research Group of the Junta de Andalucía RMN 187 is acknowledged.

REFERENCES CITED

Ashworth, J.R. (1979) Two kinds of exsolution in chondritic olivine. Mineralogical Magazine, 43, 535–538.

Arai, S. (1978) Chromian spinel lamellae in olivine from the Iwanai-Dake peridotite mass, Hokkaido, Japan. Earth and Planetary Science Letters, 39, 267–273.

Baker, J.B. and Haggerty, S.E. (1967) The alteration of olivine in basaltic and associated lavas. Part II. Intermediate and low-temperature alterations. Contributions to Mineralogy and Petrology, 16, 258–273.

Banfield, J.F., Veblen, D.R., and Jones, B.F. (1990) Transmission subsolidus oxidation and weathering of olivine. Contributions to Mineralogy and Petrology, 106, 110–123.

Beran, A. and Putnis, A. (1983) A model of the OH positions in olivine, derived from infrared-spectroscopic investigations. Physics and Chemistry of Minerals, 9, 57–60.

Berman, R.G. (1988) Internally-consistent thermodynamic data for stoichiometric minerals in the system Na_2O-K_2O-CaO-MgO-FeO-Fe_2O_3-Al_2O_3-SiO_2-TiO_2-H_2O-CO_2. Journal of Petrology, 29, 445–522.

Berman, R.G. (1991) Thermobarometry using multiequilibrium calculations: A new technique with petrologic applications. Canadian Mineralogist, 29, 833–855.

Brearley, A.J. and Champness, P.E. (1986) Magnetite exsolution in almandine garnet. Mineralogical Magazine, 50, 621–633.

Buseck, P.R. and Iijima, S. (1975) High resolution electron microscopy of enstatite. I: twinning, polymorphism and polytypism. American Mineralogist, 60, 758–770.

Buseck, P.R., Nord, G.L. Jr., and Veblen, D.R. (1980) Subsolidus phenomena in pyroxenes. In Mineralogical Society of America Reviews in Mineralogy, 7, 117–211.

Champness, P.E. (1970) Nucleation and growth of iron oxides in olivines, $(Mg,Fe)_2SiO_4$. Mineralogical Magazine, 37, 790–800.

Champness, P.E. and Gay, P. (1968) Oxidation of olivines. Nature, 218, 157–158.

Cliff, G. and Lorimer, G.W. (1975) The quantitative analysis of thin specimens. Journal of Microscopy, 103, 203–207.

Deer, R.A., Howie, R.A., and Zussman, J. (1962) Rock Forming Minerals, Vol. 1. Ortho and Ring Silicates, p. 333. Longmans, Green and Co., London.

Dobrzhinetskaya, L., Green, H.W., and Wang, S. (1996) Alpe Arami: A peridotite massif from depths of more than 300 kilometers. Science, 271, 1841–1845.

Drury, M.R. and Van Roermund, H.L.M. (1988) Metasomatic origin for Fe-Ti-rich multiphase inclusions in olivine from kimberlite xenoliths. Geology, 16, 1035–1038.

Evans, B.W. (1977) Metamorphism of alpine peridotites and serpentinites. Annual Review of Earth and Planetary Science, 5, 397–448.

Goode, A.D.T. (1974) Oxidation of natural olivine. Nature, 248, 500–501.

Gooley, R., Brett, R., Warner, J., and Smyth, J.R. (1974) A lunar rock of deep crustal origin: sample 76535. Geochimica et Cosmochimica Acta, 38, 1329–1339.

Green, H.W. and Gueguen, Y. (1983) Deformation of peridotite in the mantle and extraction by kimberlite: A case history documented by fluid and solid precipitates in olivine. Technophysics, 92, 71–92.

Green, H.W., Dobrzhinetskaya, L., and Bozhilov, K. (1997) Response to determining the origin of ultrahigh-pressure lherzolites, Science, 278, 704–707.

Hacker, B.R., Sharp, T., Zhang, R.Y., Liou, J.G., and Hervig, R.L. (1997) Determining the origin of ultrahigh-pressure lherzolites. Science, 278, 702–704.

Haggerty, S.E. and Baker, J.B. (1967) The alteration of olivine in basaltic and associated lavas. Part I. High-temperature alteration. Contributions to Mineralogy and Petrology, 16, 233–257.

Iijima, S. and Buseck, P.R. (1976) High-resolution electron microscopy of unit cell twinning in enstatite. In H.R. Wenk, Ed., Electron microscopy in mineralogy, 319–323, Springer-Verlag, New York.

Kitamura, M., Kondoh, S., Morimoto, N., Miller, G.H., Rossman, G.R., and Putnis, A. (1987) Planar OH-bearing defects in mantle olivine. Nature, 328, 143–145.

Kohlstedt, D.L. and Vander Sande, J.B. (1975) An electron microscopy study of naturally occurring oxidation produced precipitates in iron-bearing olivines. Contributions to Mineralogy and Petrology, 53, 13–24.

Martin, R.F. and Donnay, G. (1972) Hydroxyls in the mantle. American Mineralogist, 57, 554–570.

Miller, G.H., Rossman, G.R., and Harlow, G.E. (1987) The natural occurrence of hydroxide in olivine. Physics and Chemistry of Minerals, 14, 461–472.

Moseley, D. (1981) Ilmenite exsolution in olivine. American Mineralogist, 66, 976–979.

——(1984) Symplectic exsolution in olivine. American Mineralogist, 69, 139–153.

O'Hanley, D.S. (1996) Serpentinites: Record of Tectonic and Petrological History, 277 p. Oxford University Press, New York.

Otten, M.T. (1985) The subsolidus history of the Artfjället Gabbro: a TEM study of olivine, augite and orhopyroxene. Journal of Petrology, 26, 488–514.

Puga, E. (1990) The Betic Ophiolitic Association (Southeastern Spain). Ofioliti, 15, 97–117.

Puga, E., Jagoutz, E., Nieto, J.M., Díaz de Federico, A., and Ruiz Cruz, M.D. (1998) On the origin of the brown color in ALHA 77005 olivine. Lunar and Planetary Science Conference XXIX, Abstract no. 1375. Lunar and Planetary Institute, Houston (CD-ROM).

Puga, E., Nieto, J.M., Díaz de Federico, A., Bodinier, J.L., and Morten, L. (1999) Petrology and metamorphic evolution of ultramafic rocks and dolerite dykes of the Betic Ophiolitic Association (Mulhacén Complex, SE Spain): Evidence of eo-Alpine subduction following an ocean-floor metasomatic process. Lithos, in press.

Putnis, A. (1979) Electron petrography of high-temperature oxidation in olivine from Rhum layered intrusion. Mineralogical Magazine, 43, 293–296.

Risold, A.C., Trommsdorff, V., Reusser, E., and Ulmer, P. (1997) Genesis of $FeTiO_3$ inclusions in garnet peridotites from the Central Alps. Terra Nova Abstract, 9, 28–29.

Ulmer, P. and Trommsdorff, V. (1997) Titanium content of mantle olivine: an experimental study to 10 GPa. Terra Nova Abstract, 9, 39.

Veblen, D.R. and Burnham, C.W. (1978) New biopyriboles from Chester, Vermont: II. The crystal chemistry of jimthompsonite, clinojimthompsonite, and chesterite, and the amphibole-mica reaction. American Mineralogist, 63, 1053–1073.

Veblen, D.R. and Buseck, P.R. (1980) Microstructures and reaction mechanisms in biopyriboles. American Mineralogist, 65, 599–623.

——(1981) Hydrous pyriboles and sheet silicates in pyroxenes and uralites: intergrowth microstructures and reaction mechanisms. American Mineralogist, 66, 1107–1134.

Veblen, D.R., Buseck, P.R., and Burnham, C.W. (1977) Asbestiform chain silicates: New minerals and structural groups. Science, 198, 359–365.

Wilkins, R.W.T. and Sabine, W. (1973) Water content of some nominally anhydrous silicates. American Mineralogist, 58, 508–516.

MANUSCRIPT RECEIVED DECEMBER 21, 1998
MANUSCRIPT ACCEPTED JULY 28, 1999
PAPER HANDLED BY ADRIAN J. BREARLEY